PCCP

ROYAL SOCIETY OF CHEMISTRY

PAPER

View Article Online
View Journal | View Issue

Cite this: *Phys. Chem. Chem. Phys.*, 2023, **25**, 5795

Energy-dependent timescales in the dissociation of diiodothiophene dication†

Edwin Kukk, *[af] Lassi Pihlava, [a] Kuno Kooser,[ab] Christian Stråhlman, [c] Sylvain Maclot ‡[d] and Antti Kivimäki [e]

Received 12th November 2022,
Accepted 18th January 2023

DOI: 10.1039/d2cp05309h

rsc.li/pccp

Photodissociation molecular dynamics of gas-phase 2,5-diiodothiophene molecules was studied in an electron-energy-resolved electron-multi-ion coincidence experiment performed at the FinEstBeAMS beamline of MAX IV synchrotron. Following the photoionization of the iodine 4d subshell and the Auger decay, the dissociation landscape of the molecular dication was investigated as a function of the Auger electron energy. Concentrating on an major dissociation pathway, $C_4H_2I_2S^{2+} \rightarrow C_4H_2S^+ + I^+ + I$, and accessing the timescales of the process *via* ion momentum correlation analysis, it was revealed how this three-body process changes depending on the available internal energy. Using a generalized secondary dissociation model, the process was shown to evolve from secondary dissociation regime towards concerted dissociation as the available energy increased, with the secondary dissociation time constant changing from 1.5 ps to 129 fs. The experimental results were compared with simulations using a stochastic charge-hopping molecular mechanics model. It represented the observed trend and also gave a fair quantitative agreement with the experiment.

1 Introduction

Photoexcited molecular dynamics has long been an active area of research both in physical chemistry and chemical physics, both because of fundamental interest and the relevance of these processes in materials exposed to radiation, from visible light to hard X-rays. From the fundamental point of view, tracking photoinduced molecular dynamics allows stringent tests of quantum chemistry models over a broad range of conditions. Such experimental studies, many of which have been performed at synchrotron radiation sources, have gained momentum in the past decade owing to the new possibilities offered by free electron laser (FEL) radiation sources,[1–7] high-order harmonic generation (HHG)[8–15] and the development of various time-resolved techniques.[8,16–19] Consequently, there is a wealth of new information on time evolution of photoinduced molecular dynamics in small quantum systems. An interesting category of such a system is formed by thiophene, its derivatives, oligo- and polymers, since these aromatic aromatic organic compounds display a very rich photoinduced nuclear and electron dynamics.[20–27] They also have present and potential applications in, *e.g.*, molecular electronics and photovoltaics.[28–31] Another category of interest are various halogenated organic compounds, particularly the ones where hydrogen substitution by heavy elements iodine or bromine create absorption "hot-spots" for X-rays.[4,32–40] Targeting various electron shells in these hot-spots allows for versatile control in creating molecular dynamics, from intricate dissociation pathways of low-charge states to high-energy Coulomb explosions of highly charged states created by deep core ionization and/or multiphoton absorption.

In this study, we focus on the dissociation of a halogenated aromatic compound 2,5-diiodothiophene, initiated by soft X-ray ionization of iodine 4d subshell. This shallow inner-shell ionization is followed by Auger decay and the dissociation then proceeds in a dicationic electronic state. The thiophene molecule and its halogenated derivatives are know to exhibit a very rich dissociation landscape in their dicationic state, presenting an excellent model system. Furthermore, that landscape is also very dynamic, strongly dependent on the initial conditions such as the energy levels populated by the Auger decay. On the one hand, electron-energy-resolving electron-ion coincidence studies using synchrotron radiation are invaluable in relating the outcome of the dissociation, in the form of ionic and neutral fragments, to the initial conditions of the electronic structure of the parent molecule. However, such investigations

[a] *Department of Physics and Astronomy, University of Turku, FI-20014 Turku, Finland. E-mail: edwin.kukk@utu.fi*
[b] *Institute of Physics, University of Tartu, W. Ostwaldi 1, EE-50411 Tartu, Estonia*
[c] *Department of Materials Science and Applied Mathematics, Malmö University, SE-20506 Malmö, Sweden*
[d] *Department of Physics, Gothenburg University, Box 100, SE-40530 Gothenburg, Sweden*
[e] *MAX IV Laboratory, Lund University, SE-22100 Lund, Sweden*
[f] *CNRS, Laboratoire de Chimie Physique - Matière et Rayonnement, 4 Pl. Jussieu, 75005, Paris, France*

† Electronic supplementary information (ESI) available. See DOI: https://doi.org/10.1039/d2cp05309h

‡ Present address: Institut Lumière Matière UMR 5306, Université Claude Bernard Lyon 1, CNRS, Univ Lyon, 69100 Villeurbanne, France.

are by the nature of the light source not time-resolving, therefore tracking the *time-evolution* of the dissociation pathways is challenging. On the other hand, free electron laser sources (FELs) are excellent and direct probes into the time evolution of molecular photodynamics in the femto- and picosecond timescales. But combining both aspects – fine control over the initial conditions (*e.g.*, defining the dicationic electronic state), and direct time-dependent probing of the dynamics as it proceeds – is still a challenge.

Here, we present an approach to reveal time-dependent information on the dissociation pathways in a synchrotron experiment, with a precise control over the initial electronic state *via* Auger electron–ion coincidence measurement. Starting from the energetically low-lying Auger final states, the diiodothiophene molecule has a dominant three-body dissociation pathway, $RI_2^{++} \rightarrow R^+ + I^+ + I$ (R marks the thiophene ring C_4H_2S), on which we will concentrate in this study. In the time domain, such three-body reactions are commonly characterized as concerted or secondary dissociation reactions, or deferred charge separation reactions. The latter two are two-step processes with the neutral or charged iodine separating in the second step, correspondingly. We investigate this pathway covering a broad range of dicationic Auger final states and, using careful momentum correlation analysis, access the timescales of the two stages of the reaction. We will extract quantitative timescale information and show that it is strongly dependent on the amount of internal energy in the molecular dication, available for the molecular dynamics.

Following a major dissociation channel as a function of both time and energy provides a much more informative picture of the underlying processes and the essential factors governing the dynamics. Here, we use a *generalized secondary dissociation* (GSD) model, spanning the range of reactions from concerted to "pure" secondary dissociation, in the interpretation of the experiment. We also carried out a point-charge, simplified force-field, stochastic charge hopping model simulations, accessing both the energy and timescales of the molecular dynamics.

2 Experimental setup

The experiment was performed at the Finnish–Estonian beamline (FinEstBeAMS) of the MAX IV synchrotron radiation source in Lund, Sweden. The beamline[41,42] is equipped with a SX700 type monochromator manufactured by FMB Feinwerk-und Messtechnik GmbH, receiving radiation from an Apple II type undulator. Horizontally polarized radiation was used in this experiment. The 2,3-diiodothiophene ($C_4H_2I_2S$, Merck, purity $\geq$97.5%) molecules were introduced by direct evaporation from a Knudsen-cell-type crucible at a temperature of 80–100 °C. The molecular beam crossed the monochromatized photon beam at the centre of the sample region (Fig. 1). Photoelectrons were detected by a modified Scienta R4000 hemispherical electron analyzer, equipped with a fast 40 mm diameter microchannel plate (MCP) and a resistive anode (Quantar Inc.) position-sensitive detector. The electron detector provided triggers for the pulsed ion extraction voltage U_S across the source region of a modified

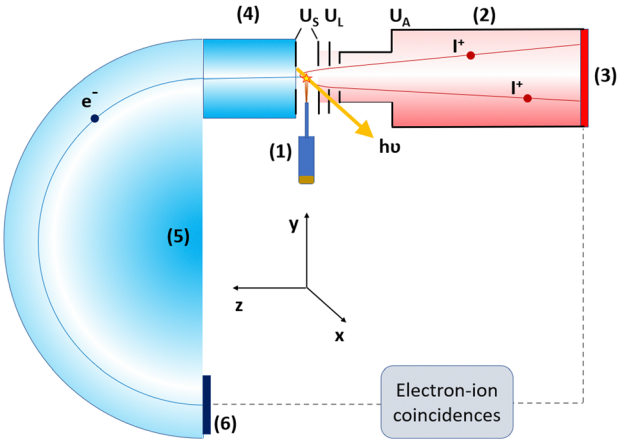

Fig. 1 Schematics of the electron-ion coincidence experiment at the gas-phase endstation. The labeled main components: (1) sample crucible and inlet, (2) ion TOF spectrometer, (3) ion detector, (4) electron lens, (5) electron analyzer and (6) electron detector.

Wiley–McLaren type ion time-of-flight (TOF) spectrometer.[43] The ions were then accelerated to the final energy by the drift tube voltage U_A, first passing a lens element with U_L, modifying the radial distribution and focusing. Ions were detected by a Roentdek 80 mm MCP and HEX-anode detector, recording ion flight times (TOFs) and radial hit positions. The electron energy and ion TOFs and ion positions of impact data were combined into a coincidence dataset. In addition, non-coincident "random" triggers for ion extraction were generated at a constant rate, interleaved with the "true coincidence" electron triggers. The ions collected using the random triggers were used for statistical subtraction of the false coincidence background from the ion TOF spectra, electron–ion–ion coincidence maps, coincident ion pair yields and ion momentum distributions.

The electron energy window for a coincidence dataset is determined by the electron acceleration/retardation and the pass energy E_p of the analyzer, its width being about 8% of E_p. Two electron-multi-ion coincidence datasets were collected, one with the Auger electron from the decay of the iodine $4d^{-1}$ vacancy created by 110 eV photons (we'll refer to it as AEPIPICO) and another with the iodine 4d photoelectron in coincidence with ions, using the 85 eV photon energy (the PEPIPICO dataset). In addition, a noncoincident ion TOF spectrum recorded at $h\nu$ = 21 eV is reported.

Pass energy of 200 eV and entrance slit of 0.5 mm was used in the AEPIPICO measurement, giving the estimated electron energy resolution of about 250 meV full-width at half-maximum (FWHM). The photon flux was adjusted to give a low average electron count rate of 24 el s^{-1}. The PEPIPICO dataset was recorded using 100 eV pass energy.

3 Experimental results

3.1 Fragmentation mass spectra

In photoinduced molecular dynamics, the dissociation landscape is primarily determined by the charge state of the molecule. Fig. 2 shows the mass spectra of diiodothiophene

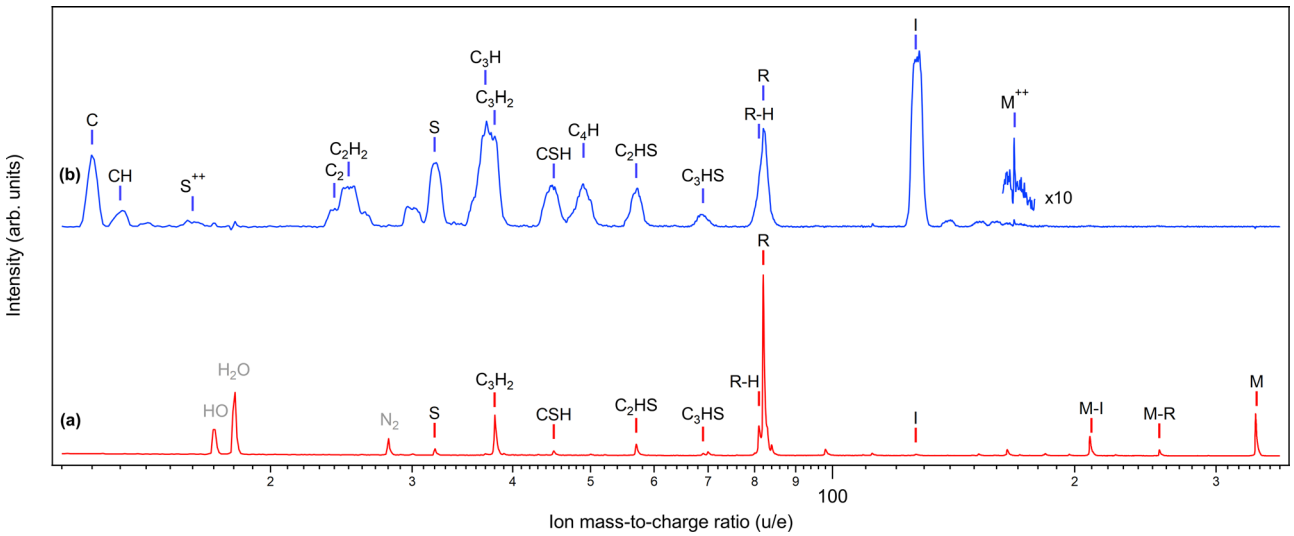

Fig. 2 Ion mass spectra recorded at two ionizing photon energies: (a) $h\nu$ = 21 eV and (b) 85 eV. Spectrum (a) is converted from a noncoincident ion time-of-flight spectrum. Spectrum (b) was measured in coincidence with the iodine 4d photoelectrons and contributions from other ionization channels were subtracted using the random-triggered spectrum. Vertical lines and labels denote various fragments, with M standing for the parent molecule and R for the thiophene ring C_4SH_2. All fragments are singly charged unless marked otherwise.

for singly charged (a) and doubly charged (b) parent molecule, the first following valence ionization and the second resulting from iodine 4d ionization and subsequent Auger decay of the I $4d^{-1}$ inner-shell hole state (see also Fig. 3). The spectra are converted to the mass/charge scale from the original time-of-flight (TOF) measurement and the various species are labeled in Fig. 2. Throughout the paper, M refers to the parent molecule $C_4H_2I_2S$ and R to the thiophene ring fragment C_4H_2S. Under valence ionization conditions, the singly charged parent molecule has a considerable survival probability. If dissociation occurs, it is prevalently *via* the ejection of neutral iodine(s), producing the $(M–I)^+$ and the thiophene ring R^+ fragments. The latter is accompanied by a hydrogen loss peak. Additional fracturing of the ring fragment can also occur, producing ions such as $C_3H_2^+$. Note that the possible proton fragments fall outside the measurement range and the peaks below the S^+ peak arise from the rest-gas due to the sample temperature and density being kept low.

Spectrum (b) is the result of dissociation of a wide range of dicationic electronic states populated by the Auger decay of the $4d^{-1}$ state. In contrast to the valence-ionized spectrum (a), iodine cation ejection now occurs and it is the strongest detected fragment, followed by the intact thiophene ring (including hydrogen loss(es)). The ring fractures now, however, with a much higher probability, creating essentially all possible ring fragment ions. The peaks (except M^{++}) in spectrum (b) are broadened compared to the ones in spectrum (a), due to the Coulomb repulsion between fragments, resulting in high fragment momenta. There is also a very small probability of creating stable parent dications (M^{++}) in spectrum (b). The unlabelled peak at *M* = 30 u is likely NO^+ and, as it appears in coincidence with I^+, is due to nitrosyl iodide impurity.

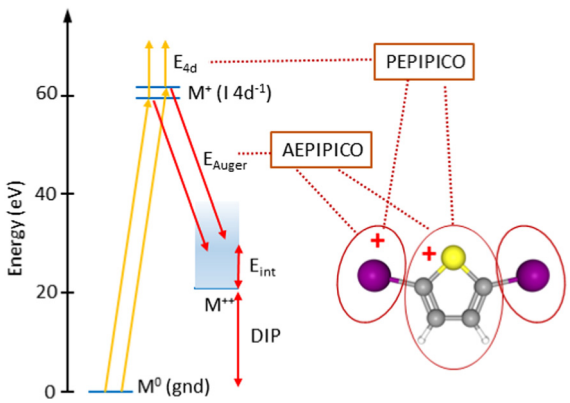

Fig. 3 Energy schematics of the photoionization and Auger decay processes prior to the dissociation. To the right is sketched the main three-body dissociation pathway of diiodothiophene. The PEPIPICO and AEPIPICO labels define the measured coincidence datasets with I 4d photoelectrons and Auger electrons, respectively.

3.2 Ion–ion coincidences, dissociation pathways and ion pair yields

A more detailed picture of the dissociation pattern of multiply charged molecules is obtained by coincident analysis of the emitted ions. Fig. 4 shows the ion pairs in the PEPIPICO dataset, detected in coincidence with the iodine 4d photoelectrons. They are presented in the form of an ion–ion coincidence (PIPICO) map, where the flight times of the faster and slower ionic fragments in the ToF spectrometer are given by the *x* and *y*-axis, respectively. The number of ion pairs is color-coded in the 2D histogram. The third particle – the photoelectron detected in coincidence – acts as a filter in this presentation, allowing only the dissociation events arising from the 4d ionization. There is, however, a chance of combining electrons and ions from different ionization events, if those occur sufficiently close in time. Such "false" coincidences were subtracted from the PIPICO map

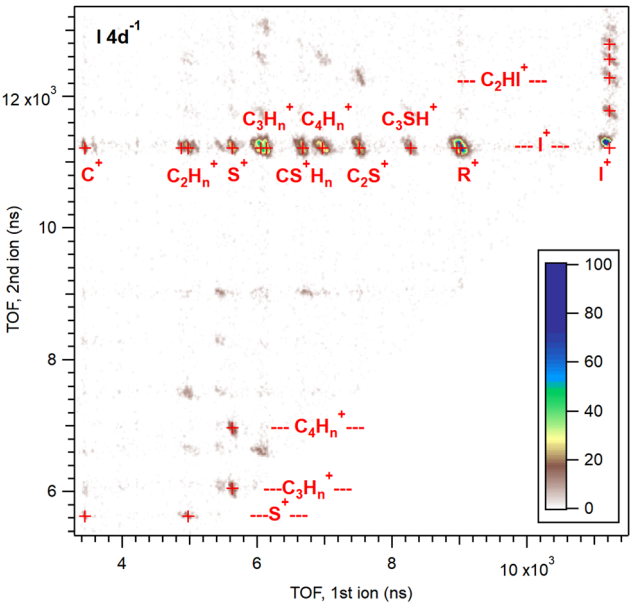

Fig. 4 Electron–ion–ion coincidence (PEPIPICO) map, recorded in coincidence with the I 4d photoelectrons at the photon energy of 85 eV. False coincidence background has been subtracted. Red markers denote the centre positions of the patterns and the labels indicate the identification of fragments on the horizontal and vertical axis.

using a random-triggered dataset measured simultaneously as interleaved with the electron triggers. A precise false background subtraction from a histogram representing a multi-particle coincidence requires a number of parameters to be known about the detection efficiencies *etc.*[44] Here, we applied a more empirical technique where background PIPICO maps were constructed from (a) the random-triggered data and (b) combining ions from electron- and random-triggered data. These maps were then subtracted from the electron-triggered map, fine-tuning the multiplication coefficients by checking the intensity of the features that can only be false coincidences. For what will be our main region of interest, the (R^+,I^+) ion pairs, the coincidence purity was the following: 26 times more (R^+,I^+) ion pairs were produced in coincidence with the I 4d photoelectrons than by random triggers; 6.8 times more in coincidence with the Auger electrons (E_{kin} = 26–32 eV).

Various ion pairs form islands in the PIPICO map, as labeled in Fig. 4. The most abundant fragment in Fig. 2, I^+, combines with all other ionic fragments, but most prominently with the intact thiophene ring R^+. In addition, the map contains weak patterns with both charges localized to the ring fragments and two neutral iodines ejected. The top quarter of the map contains pathways where one iodine remains attached to the ring or ring fragments. Outside the region shown, there are a few very weak two-body dissociation channels, (I^+,RI^+) and $(C_nH_mI^+,C_{4-n}SH_{2-m}I^+)$.

In the PIPICO map, the patterns for each ion pair are bar-shaped with a negative slope. The flight time of an ion increases from its nominal value (for the ion initially at rest), if the initial momentum from the dissociation points away from the ion detector (see Fig. 1), and decreases if the initial momentum is towards the detector. In a two-body dissociation, the momenta of the two ions are strictly antiparallel, therefore if the first ion's flight time decreases, the flight time of the second ion increases and *vice versa*. The slope of the pattern (in that case −1) thus represents the momentum correlation between the fragment ions. Note that the (I^+,I^+) pair exhibits only a half-pattern above the diagonal in this presentation.

The PIPICO map in Fig. 4 presents an overall dissociation landscape associated with the I 4d ionization. By measuring these fragment ions in coincidence with the *Auger* electrons, one would obtain a much more differential picture with the dissociation landscape changing as different Auger final electronic states are populated (see Fig. 3). First, the top panel of Fig. 5 shows a noncoincident Auger electron spectrum following the I 4d ionization. The spectrum covers an about 30 eV range of the final dicationic states and the highest energy of the Auger electrons corresponds to the lowest possible energy of the final dicationic state M^{++}. The energy of that state, relative to the neutral ground state, is the double ionization potential (DIP, Fig. 3).

It is difficult to locate this energy value in the electron spectrum, since the Auger intensities to the low-lying dicationic states can be quite weak. Therefore, we used the coincident ion

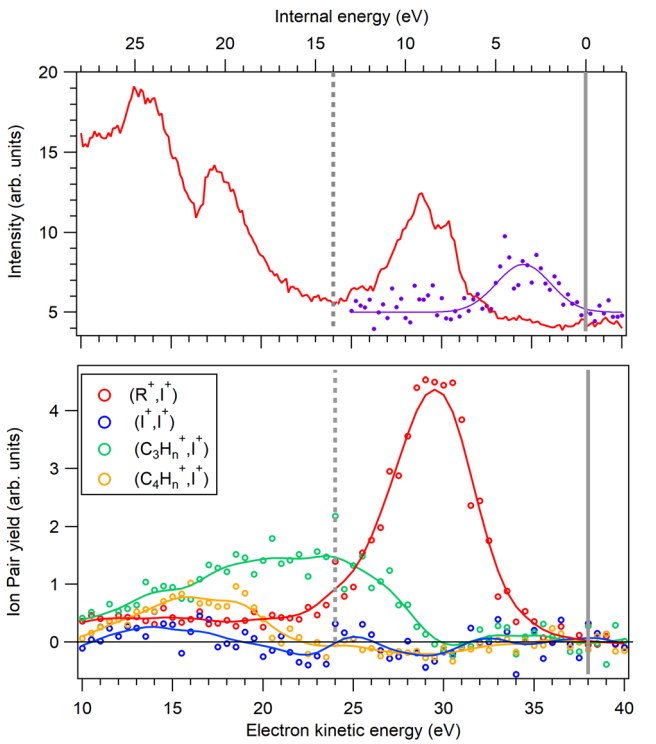

Fig. 5 Top: Auger electron spectrum of the decay of the I $4d^{-1}$ state, from the AEPIPICO measurement. The dashed vertical line marks the boundary between the two datasets with a different electron energy window. The spectrum is corrected for the analyzer's transmission. Dots with a Gaussian fitline show the yield of the doubly charged parent molecule and the gray vertical line marks the double ionization potential (DIP). Bottom: Yields of the ion pairs that form the major channels in the PIPICO map. Estimated false coincidence contributions and a true ion pair background was subtracted and the left-hand curves were multiplied by a factor of 1.2 for joining the two energy windows.

yield (CIY) of the M^{++} ions with the Auger electron for DIP determination. M^{++} is the first ion to appear in the mass spectrum as the lowest M^{++} states are populated; as the internal energy increases, fragmentation becomes possible and the M^{++} signal disappears. From the right-hand slope of the M^{++} CIY curve in Fig. 5(top), we determined the DIP to be 22.6 eV above the neutral ground state energy, corresponding to 38.0 eV Auger electron's energy. DIP defines the origin of the the internal energy scale (the top axis). An inherent uncertainty in the correspondence between the Auger electron energy, DIP and the internal energy E_{int} arises because of the 1.7 eV spin–orbit splitting of the I $4d^{-1}$ state. The Auger spectrum therefore consists of two replicas, shifted by 1.7 eV, which imposes the uncertainty of the experimental internal energy scale.

Let us now turn to various other ion yields in the lower panel of Fig. 5. Since the dicationic dissociation pathways are much better defined by the ion pairs than single ions, we extracted coincident ion pair yields (CIPYs) as a function of the Auger electron energy, and consequently also as a function of the internal energy. The lower panel of Fig. 5 shows the CIPY curves of some of the most prominent ion pairs seen in the PIPICO map of Fig. 4. Since in the AEPIPICO measurement, the electron energy window was limited to about 16 eV, two separate datasets were recorded in order to cover the entire Auger spectrum. The datasets were joined together for the CIPY curves in Fig. 5, with the dataset separation energy shown as the dashed vertical line. One can see that, moving in the direction of increasing internal energy, after the M^{++} signal disappears, the first dissociation channel to open is (R^+,I^+). At higher internal energies, the ring starts to fragment, thus suppressing the (R^+,I^+) CIPY. The (I^+,I^+) CIPY is quite weak in the covered energy region, but it was a strong pattern in the overview PIPICO map. This is explained by (I^+,I^+) being a high-energy dissociation pathway, that only opens up at the high internal (low electron kinetic) energies that are to the left of the detected Auger electron energy windows in Fig. 5.

3.3 Timescales of the main dissociation pathway

3.3.1 Slope analysis. Let us now concentrate on the major three-body pathway $RI_2^{++} \rightarrow R^+ + I^+ + I$, represented by the (R^+,I^+) CIPY in Fig. 5. Its pattern in Fig. 4 has a slope of −1.70(6), or the tilt angle of about 30° from vertical. As described above, the pattern's slope reflects the momentum sharing between the fragments. Specifically, it reflects the deviation of the TOF of ions from their nominal flight time, that is proportional to the p_z component (along the axis of the spectrometer) of their momenta. The other two components of the momenta determine

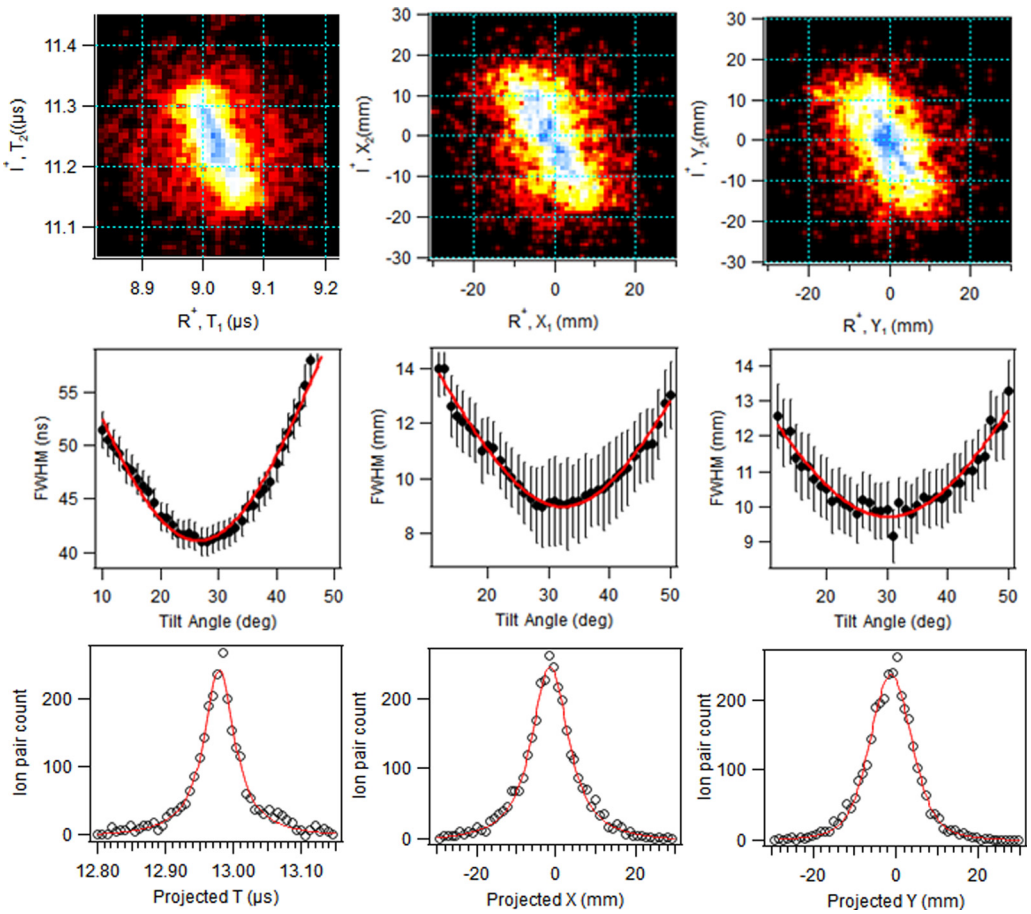

Fig. 6 AEPIPICO pattern slope analysis for the (R^+,I^+) ion pair. Top row: PIPICO patterns in the *T*, *X*, and *Y* coordinates. Middle row: Width of the projected patterns as a function of the tilt angle. Bottom row: Projected distributions after rotation of the PIPICO patterns by the tilt angle corresponding to the narrowest width. Red lines are least-squares curve fits.

the hit position of the ions on the position sensitive detector, where the deviation from the center is also proportional to the components p_x and p_y. One can therefore carry out the slope analysis not only for T_I *vs.* T_R patterns as seen in the PIPICO maps in the TOF scale (Fig. 4), but also for the X_I *vs.* X_R and Y_I *vs.* Y_R position patterns. We found this analysis to be more reliable than direct comparison of the momentum vector magnitudes, as calculated from the $\Delta T = T - T_n$ (T_n is the nominal flight time of the ions with no initial momentum), X and Y values, and providing also redundancy for verification. It is of more interest to apply the accurate slope analysis not to the overview PEPIPICO map of Fig. 4, but to the AEPIPICO maps generated in coincidence with the Auger electrons. Such maps can be generated for any subset of coincidence events with a given range of the the Auger electron energy, allowing to follow the possible dependencies of the ion momentum sharing on the internal energy E_{int} of the parent dication (Fig. 3). First, as a illustration, Fig. 6 shows a 3D slope analysis of the (R^+,I^+) pattern for those events with the Auger electron energy between 30 and 32 eV. This internal energy range, from 6 to 8 eV is characterized by complete dominance of the $RI_2^{++} \rightarrow R^+ + I^+ + I$ pathway (see Fig. 5(bottom)). The top row of Fig. 6 shows the PIPICO pattern of this process, corresponding *only* to the Auger electrons in the above energy range. The pattern appears in both the time and position coordinates for the (R^+,I^+) ion pair. Using coordinate rotation, we then changed the tilt angle of the pattern and projected it down to the x-axis. The projection is a one-dimensional spectrum in mixed 1st and 2nd ion coordinates (T, X, or Y) and, since the patterns are elongated, it exhibits the narrowest peak width when the tilted pattern becomes vertical. The middle row shows a scan over a range of tilt angles, with the projection peak widths determined at each angle. The FWHM(tilt angle) curves were then fitted with a cosine + sine type function that geometrically represents the projection of a tilted rectangular shape. One can see that all three curves display a clear minimum position, the fitted value of which was taken as the tilt angle of the pattern. The bottom row shows the projected spectra after rotating the patterns by the tilt angle to vertical position. The X and Y coordinate projections were fitted by Voigt functions for width determination. The flight time projections have a complication that the pattern can contain also events with $(R–H)^+$ and $(R–H2)^+$ ions that would create a shoulder in the left-hand side of the projected spectrum, possibly distorting the determination of the tilt angle. We therefore used a three-peak fitting function with predetermined peak spacing to account for multiple ions with different masses. However, no significant differences were observed compared to the standard fit with a single Voigt profile.

Before reporting the experimental findings on momentum sharing in the (R^+,I^+) pattern, let us introduce the *generalized secondary dissociation (GSD) model* as a means of interpretation.

3.3.2 Generalized secondary dissociation model. In many-body dissociation, the pattern's slope is an indication of the momentum division between the fragments in the various stages of the dissociation. In the following, we apply a two-step dissociation model to the $RI_2^{++} \rightarrow R^+ + I^+ + I$ pathway with the assumption that momentum exchange occurs only between the charged fragments due to Coulomb repulsion. The three basic scenarios are then: (i) the neutral I fragment separates in a concerted three-body dissociation process, it acquires no momentum and the two ions behave as if originating from a two-body process with a PIPICO slope of -1. If the separation is not simultaneous but step-wise, there are two possible branches, (ii) the neutral I fragment separates before the dissociation of RI^{++} into R^+ and I^+ – the deferred charge separation. Also in that case, the expected slope is -1. (iii) The neutral I fragment separates from the ring after the dissociation of RI_2^{++} into I^+ and RI^+ – the secondary dissociation. In that case, the neutral I fragment acquires momentum during the first stage, while part of the RI^+ fragment. If the secondary dissociation then occurs at an infinitely large distance from I^+, the expected slope of the (R^+,I^+) PIPICO pattern is given by the mass ratio:

$$\frac{dT_I}{dT_R} = -\frac{M(RI^+)}{M(R^+)} = -2.55.$$

Thus, the basic description for the two-step three-body dissociation predicts the PIPICO slope of either -1 or -2.55, or the tilt angles of 45° and 21.4°, respectively. The tilt angle in the overview PIPICO map was 30.5°. It thus conforms to none of the three scenarios.

An obvious way to improve the model is by introducing a finite secondary dissociation distance in the process (iii), making a smooth transition from concerted to secondary dissociation. The momentum sharing and the resultant slope of the PIPICO pattern can be calculated knowing the masses of the charged fragments in the first stage:

$$RI_2^{++} \rightarrow I^+ + RI^+,\ M(I^+) = 127\ u,\ M(RI^+) = 209\ u$$

and in the second stage:

$$RI^+ \rightarrow I + R^+,\ M(I) = 127\ u,\ M(R^+) = 82\ u.$$

In addition, the initial separation of the I^+ and RI^+ fragments for the first stage is needed. We used 4.07 Å, the distance between I^+ and the weighted centre of the RI^+ fraction in the initial geometry, with weights according to the number of possible atomic valence vacancies. The variable in the model is the separation between the I^+ and RI^+ fragments at the moment of the secondary dissociation T_{sec}. Fig. 7 shows the relationship between the PIPICO pattern's tilt angle and T_{sec}, *i.e.*, evolution from concerted to "pure" secondary dissociation in the GSD model. For example, the experimental tilt angle of 30° of the (R^+,I^+) pattern in the overview map in Fig. 4 corresponds to the secondary dissociation distance of 7.5 Å, which is reached in T_{sec} = 286 fs after the I^+, RI^+ charge separation. It should be noted that the model is quite sensitive to the initial distance parameter: using the unweighted mean of the atomic coordinates of the RI^+ fragment gives about 0.25 Å shorter distance and a 25 fs smaller value for T_{sec}; a change of the initial distance by 1 Å gives about a 100 fs change in T_{sec} at this particular slope angle.

The GSD model predicts also the magnitudes of the momenta of the dissociation products, and as a consistency check, they are compared with the experimental momentum

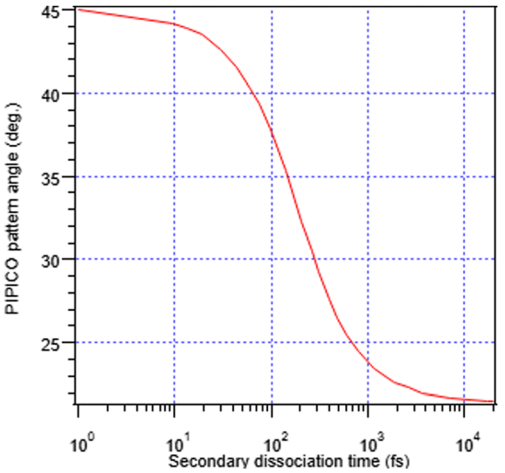

Fig. 7 Predictions of the generalized secondary dissociation model of the (R^+,I^+) pattern's tilt angle, as a function of the secondary dissociation time T_{sec}. The left- and right-hand limits correspond to the concerted and "pure" secondary dissociation cases.

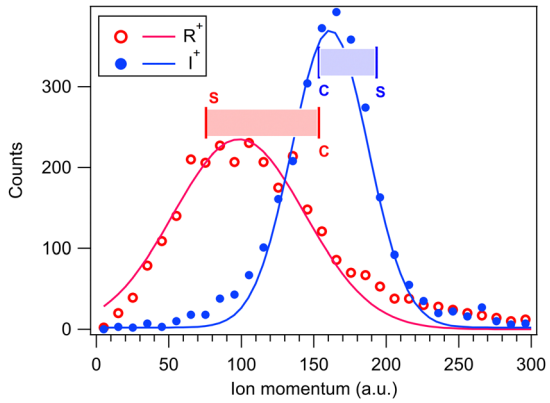

Fig. 8 Momentum distributions of the R^+ and I^+ ions in the (R^+,I^+) ion pair, coincident with the I 4d photoelectron. Solid lines are Gaussian fits. Vertical bars denote the momentum values predicted by the GSD model for the "pure" sequential (S) and concerted (C) three-body dissociation.

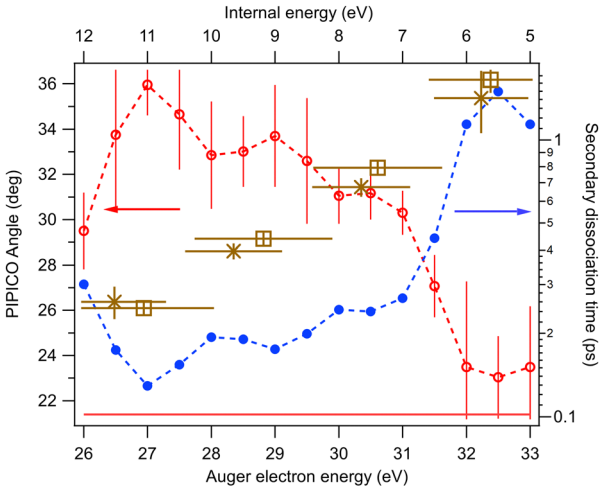

Fig. 9 Tilt angle (red open circles) of the experimental PIPICO pattern for the (R^+,I^+) ion pairs as a function of the Auger electron energy and the internal energy E_{int} of the parent dication. The corresponding secondary dissociation time constant T_{sec} (blue dots) is calculated using the generalized secondary dissociation model. The horizontal line shows the limiting tilt angle for "pure" secondary dissociation. The limiting angle for the concerted dissociation and deferred charge separation is 45°. Brown markers (×,□) with error bars show the secondary dissociation times $T_{1/2N}$ from simulations (see Section 4 for details).

distributions from the PEPIPICO dataset in Fig. 8. The curves were extracted from (R^+,I^+) ion pairs and show quite broad momentum distribution for the R^+ fragment and a narrower one at higher values for I^+. Also marked at the figure are the GSD model values at the concerted and "pure" secondary dissociation limits, calculated using the I^+,RI^+ initial separation of 4.07 Å. The shaded ranges correspond to the transition region, where the R^+ momentum increases and I^+ momentum decreases. As can be seen, these ranges fit very well with the observed distributions.

3.3.3 Secondary dissociation timescales and dependency on the internal energy. We can now return to the slope analysis results of the AEPIPICO data. They are shown as red circles in Fig. 9 as the tilt angle of the (R^+,I^+) pattern from subsets of the AEPIPICO data, for various ranges of the Auger electron kinetic energy. The corresponding internal energy range is given by the top axis. The datapoints are averages of the three values obtained from the AEPIPICO patterns constructed using the flight time and the x and y coordinates. The data error bars reflect both the statistical uncertainty and the variations when using different fitting models for determining the tilt angle that gives the narrowest projected PIPICO pattern.

One can see that at the lowest internal energies, near the appearance threshold of the (R^+,I^+) ion pair (Fig. 5), the angle approaches that of "pure" secondary dissociation (dashed horizontal line), where $T_{sec} \rightarrow \infty$. The blue dots show the corresponding secondary dissociation times T_{sec}, as calculated from the GSD model (Fig. 7). In the low-internal-energy region, T_{sec} reaches 1.5 ps. It then decreases as the tilt angle increases with the internal energy. The largest angle, 36°, corresponds to T_{sec} of about 130 fs, approaching the faster process of concerted dissociation. At the highest internal energies, $E_{int} > 10.5$ eV, the tilt angle decreases again, although we note that in this region the PIPICO pattern has become quite diffuse and the tilt angle determination less accurate. This would be an unexpected behaviour, unless we consider the entire dissociation landscape. At around this energy, the next fragmentation pathway, the ion pair $(C_2H_n^+,I^+)$ (Fig. 5), opens up. Here, the ring itself fragments: $R^+ \rightarrow C_2H_n^+ + C_2SH_{2-n}$. Other factors than the internal energy, such as the electronic nature of the dicationic state of the parent molecule, may influence, which pathway the dissociation embarks on. Then there can be a subset of the initial ensemble following the slow $RI_2^{++} \rightarrow R^+ + I^+ + I$ pathway and another, "fast" subset branching out into the more energetic 4-body pathway. Thus, opening up a new dissociation pathway may explain the reversal of the three-body pathway towards the slower secondary dissociation.

In general, the main experimental finding is the continuous change of the $RI_2^{++} \rightarrow R^+ + I^+ + I$ process from nearly pure

secondary dissociation as the pathway becomes energetically possible and opens, towards a faster, concerted three-body process as the available energy increases.

4 Computational simulations of dissociation timescales and comparison with experiment

In reality, even under precisely determined initial conditions, the C–I bond breakage times obviously vary from event to event; a statistical aspect that the analytical GSD model is not able to reproduce. In order to create a statistically more realistic description, we developed further the point charge Coulomb explosion model from earlier studies[36,45] that has been specifically designed to simulate statistical distributions of experimentally measurable quantities – fragment charges, momenta and their correlations. There are many more advanced computational molecular dynamics tools,[24,25,46–49] that give a much more accurate representation of the dynamics within the range of the molecular field, but are severely limited in determining the asymptotic behaviour of dissociation such as the charge localization and, consequently, the momenta obtained by the fragments. The model as presently applied is a stochastic charge hopping molecular mechanics model with simplified force field of molecular bonding. This light approach is focused on the asymptotic result and allows to generate large datasets directly comparable with the experiment. The detailed description and the used parameters are given in the ESI,† but the essential elements in modeling the fragmentation dynamics are:

1. Atoms are treated as point charges with integer values (0, +e, +2e). The total molecular charge was +2e and the initial allocation of the charges was randomized, giving a basic representation of the broad range of the final states of the Auger transitions.

2. The +e unit charges are allowed to hop across the bonds between atoms during the dynamics. The hops are cut off at a critical distance given by the classical over-the barrier model.[35]

3. The molecular bonds are described by a simplified force field that includes the bond stretching and bending vibrations. For our purposes, obtaining and maintaining the optimum molecular and fragment geometries is not the primary objective; instead, the force field should be suited for realistic bond breakage description. Therefore, Morse potential energy curves were chosen to describe the bonds. Bending vibrations were included using a common force constant and the equilibrium angles were chosen either from the initial geometry of the molecule or as a linear geometry of the opened thiophene ring. The latter choice was made for the simulations reported here, due to supporting experimental and theoretical findings.[21,22,24,25,50,51] Optionally, the bending force constant was also applied to restrict deviation of bonds from the initial plane of the molecule. No torsional forces were included. As non-bonding interactions, a repulsive potential wall was created around atoms.

At the start of the dynamics, the molecule was given internal energy, in addition to the potential energy of the coulombic repulsion of point charges. It is in the form of randomly distributed atomic velocities (internal temperature). Randomization for simulated datasets was obtained by (i) choice of the initial atomic velocities, (ii) initial charge localizations and (iii) redistributing charges across bonds during the hops.

First, let us confirm whether the stochastic charge hopping molecular mechanics model gives a reasonable statistical description of the overall dissociation landscape. Fig. 10 shows a comparison of a simulated PIPICO map with the experimental one. The fragment mass and charge values together with the p_z projections of their momenta were converted to the ion TOF values, using the conversion factors corresponding to our experimental conditions. The ion momenta were obtained in the fixed frame-of-reference for the Monte Carlo dataset of trajectories, but random, isotropic frame rotation was then applied for each trajectory in order to simulate the isotropic orientation of the gas-phase molecules in the experiments. The simulation was run with E_{int} = 7 eV initial energy. However, charge hopping in this point-charge model tends to create a drift towards higher internal energies, due to the molecule starting to accommodate its geometry to a particular charge configuration between the hops, which then tend to bring the molecule into an energetically less favourable geometry. This slight random drift causes the trajectories to be generated for a range of eventual internal energies. Although at first glance a completely unphysical feature, such energy drift can in fact be regarded as a basic representation of internal energy conversion, where the seemingly external energy source would be the relaxation of the electronic structure that is not a part of this model. Here, only the trajectories with the internal energy less than 9 eV were selected for generating the left-hand PIPICO map in Fig. 10. As noted above, the equilibrium C–C–C, C–C–S and C–S–C bond angles of a linear geometry were chosen, and the trajectories therefore started from a non-equilibrium cyclic geometry. Equivalent simulations were run with the equilibrium bond angles of the ring structure; no significant differences in the outcome as the PIPICO map were found.

The right-hand side shows the experimental AEPIPICO map constructed from the events with the Auger electron energy E_{kin} = 29–32 eV (E_{int} = 6–9 eV). Note that this experimental map is quite different than the overview PEPIPICO map in Fig. 4, since the latter, measured in coincidence with the I 4d photoelectrons, includes all Auger transitions. The experimental map shows faint horizontal and vertical bands, especially associated with the strongest fragment ions I^+ and R^+. These are due to residual false coincidence events. Both have the (R^+,I^+) pattern as the dominating one, followed by the weaker (I^+,I^+) pattern. In contrast to the overview PEPIPICO map, here all other patterns are of much less intensity. These are, however, present in both the simulated and experimental map. The simulation also has a very weak two-body pattern (C_2HI^+,C_2SHI^+) in the top-right corner of the map; it is unobservable in the experimental map. The excess heavy-fragment patterns in the simulations is most likely due to the limited integration time (2 ps), as secondary dissociation events would slowly deplete these patterns, were the simulation to continue.

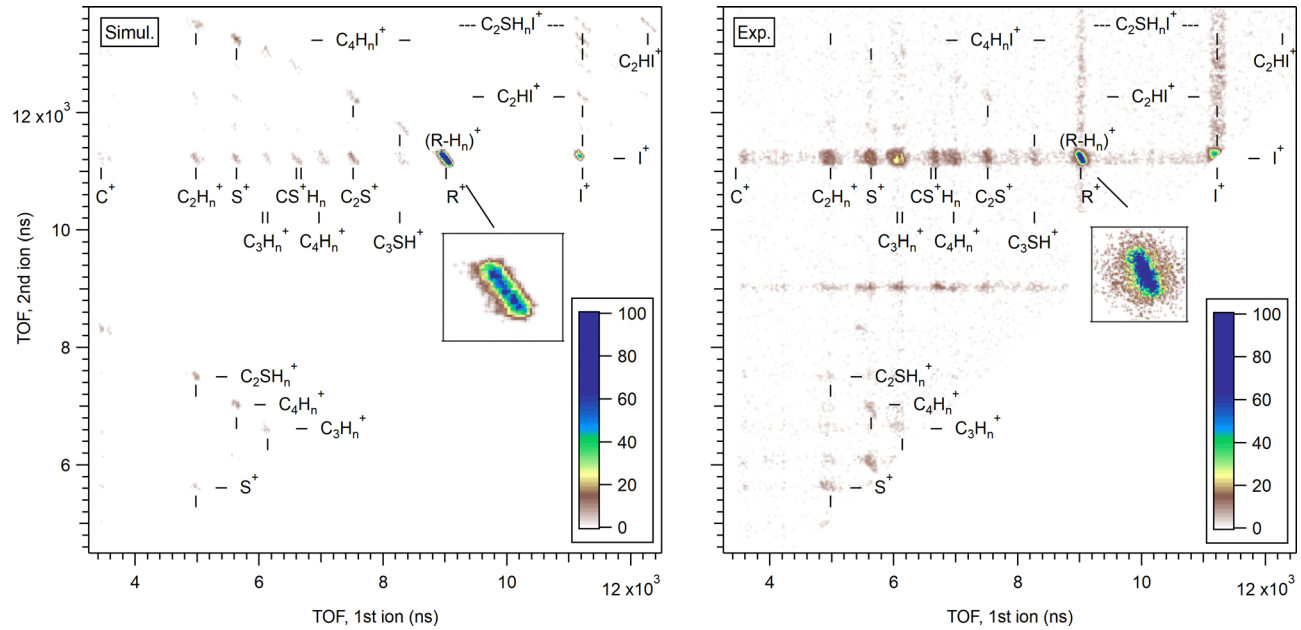

Fig. 10 Comparison between modelled (left) and experimental (right) PIPICO maps for dicationic dissociation of diiodothiophene. The Monte Carlo simulation was carried out at E_{int} = 7 eV and with the optimum opened-ring geometry. The experimental map is constructed from PEPIPICO coincidence events with the I $4d^{-1}$ Auger decay electrons, limiting their energy range to E_{kin} = 29–32 eV. Approximate false coincidence background was subtractred using random-triggered coincidences. The insets show the (R^+,I^+) pattern in more detail.

Let us now concentrate once again on the main pathway of interest, $RI_2^{++} \rightarrow R^+ + I^+ + I$. The insets of Fig. 10 show the corresponding PIPICO pattern for both the simulated and experimental dataset. It appears to have a larger slope in the latter, suggesting that the simulation is not well describing the momentum sharing. However, this discrepancy is explained below after scrutinizing the time information from individual trajectories. While for the experiment, the secondary dissociation time T_{sec} was deduced from the tilt angle of the (R^+,I^+) pattern using the GSD model, in the simulation the bond breakage times are directly available from each trajectory. Fig. 11 shows the histogram of the I–C bond breakage times, for yielding both the charged and neutral atomic iodine fragments. Same as for the PIPICO map, the analyzed trajectories were restricted to the $E_{int} < 9$ eV range.

The simplest statistical description of these distribution functions is that of constant-rate, exponential decay. The distributions from the simulation were fitted with a delayed exponential function, the delay occuring due to the minimum time required to reach the bond breakage distance. The decay time constants τ_P = 366(14) fs and τ_N = 974(75) fs were obtained for the ejection of charged and neutral iodine fragments, respectively. It can thus be seen that in the simulation, the neutral iodine separation is a significantly slower process. The difference between the neutral and charged iodine separation times from the ring gives the secondary dissociation time T_{sec} in each trajectory and the corresponding histogram is also shown in Fig. 11. Trajectories in the histogram at T_{sec} = 0 are concerted dissociation and at $T_{sec} > 0$ develop into secondary dissociation. There is also a large number of trajectories with $T_{sec} < 0$ that represent deferred charge separation.

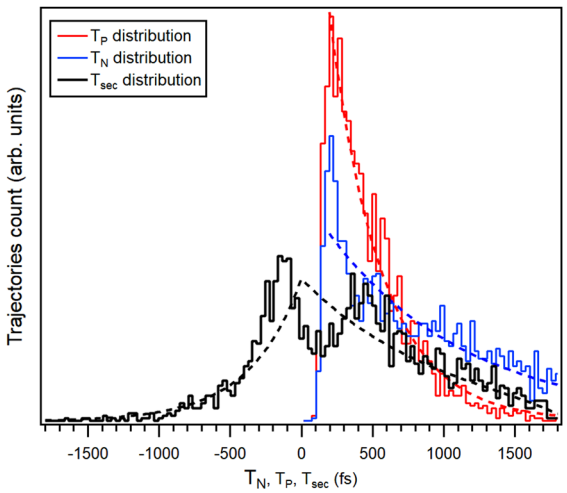

Fig. 11 Time distributions of the C–I bond breakage events in the simulated trajectories with E_{int} = 7 eV, for neutral (blue) and charged (red) iodine separtion. Colored dashed lines are fits by exponential decay function. The black curve is the distribution of the trajectories by the secondary dissociation time T_{sec} and the black dashed line is the distribution obtained by eqn (1).

The basic assumption regarding the the two iodine separation events can be either that they are independent or that they are correlated, such as when the first bond break significantly changes the likelihood of the second bond breakage within a certain time period. Let us consider the former, simpler case.

We mark the probability distribution function of the neutral and charged iodine separating as $f_N(t;t \geq 0)$ and $f_P(t;t \geq 0)$, respectively. Then, the probability that the second bond break occurs after time T_{sec} is given as

$$p(T_{sec}; T_{sec} \geq 0) = \int_0^\infty f_P(t) f_N(t + T_{sec}) dt,$$
$$p(T_{sec}; T_{sec} < 0) = \int_{-T_{sec}}^\infty f_P(t) f_N(t + T_{sec}) dt. \quad (1)$$

Here, the positive T_{sec} values would correspond to the secondary dissociation branch and the negative T_{sec} values to the deferred charge separation branch. Assuming that both bonds break independently following the exponential decay law with characteristic decay times τ_P and τ_N, we obtain the distribution functions for the secondary dissociation and deferred charge separation branches:

$$p(T_{sec}; T_{sec} \geq 0) = \frac{1}{\tau_N + \tau_P} e^{-\frac{T_{sec}}{\tau_N}}$$
$$p(T_{sec}; T_{sec} < 0) = \frac{1}{\tau_N + \tau_P} e^{-\frac{T_{sec}}{\tau_P}} \quad (2)$$

Fig. 11 also shows the secondary dissociation time distribution, calculated using eqn (1) and the fitted exponential decay time constants. As seen, the asymptotic behaviour reaching the deferred charge separation and the "pure" secondary dissociation limits is well described by independently occuring neutral and charged iodine separations, with their respective rate constants. In the region near the concerted dissociation, $|T_{sec}| < 500$ fs, the simulations exhibit significant correlation between the two events. Namely, by suppressing the separation of the second iodine, whether neutral or charged, for up to $\approx$200 fs after the first event and with the corresponding pile-up at $\approx$200–400 fs. However, we are reluctant to ascribe a physical relevance to these correlation features without further studies. Furthermore, the entire deferred charge separation wing of the distribution cannot be confirmed by experimental data. All the trajectories with T_{sec} negative or zero contribute as PIPICO patterns with the tilt angle of 45° and constitute about 36% of the simulated trajectories in the $E_{int} <$ 9 eV range. The basic charge hopping model used in the simulations allows for charge location and delocation on the iodine atoms with fixed probability up to the C–I bond length at which the Coulomb barrier is reached (5.51 Å), dropping abruptly to zero after that. Due to lack of experimental evidence, we regard the deferred charge separation branch at this stage of the model development, as a possible model artefact. This also explains the difference in slopes of the simulated and experimental PIPICO patterns, as the slope of the simulated pattern, with the trajectories with $T_{sec} < 0$ discarded, becomes steeper.

Lastly, we note that the exponential time constants τ_N and τ_P are not the best measure to compare with the GSD model values from the experiment, since about 63% of the events occur before that time. We therefore use the "half-life" value $T_{1/2} = \ln 2 \times \tau$: $T_{1/2P}$ = 254(10) fs and $T_{1/2N}$ = 675(52) fs, where the error bars reflect the confidence level of the exponential fit.

Similar simulations and and the time analysis of the $RI_2^{++} \rightarrow R^+ + I^+ + I$ pathway was carried out for a number of internal energies, E_{int} = 3, 5, 7, 9 and 11 eV. The secondary dissociation times T_{sec} thus obtained are plotted in Fig. 9 together with the T_{sec} values derived from the Auger electron–ion–ion coincidence experiment. The two sets of simulated values differ by the absence (×) or presence (⊡) of forces returning the atoms to the molecular plane. The predictions of the model for the secondary dissociation time fit well with the 100 fs to 1 ps timescale range of the experiment. A closer look at the modeled trajectories shows that the C–I bond breaks do not occur at a particular point in the evolution of the overall geometry, but are described more as a statistical process due to fluctuating internal energy and Coulomb repulsion. The stochastic molecular mechanics model used here included the strongest vibrational interactions – bond stretching and bending – with the highest capacity to store the high amount of internal energy. While a more advanced modeling can well achieve a better quantitative agreement with the experiment, it is unlikely that low-energy vibrational modes such as torsional motion significantly affect the characteristic timescales of the dissociation reaction.

When the simulated $\ln(1/T_{sec})$ values are plotted against $1/E_{int}$, they follow a linear trend. In accordance to the Arrhenius equation, the slope of that trend is the activation energy of the reaction and from a linear fit, we obtained the activation energy value as 20 eV. This is much higher than the C–I bond dissociation energy, which in the model was taken as 1.78 eV. This large difference indicates that even in our quite simple model, the bond breaks cannot be statistically reduced to simply the issue of average internal energy in a degree of freedom *vs.* bond dissociation energy.

5 Conclusions

A detailed momentum correlation analysis of the main dicationic dissociation pathway of 2,5 diiodothiophene, $RI_2^{++} \rightarrow R^+ + I^+ + I$, allowed us to retrieve quantitative time-scale information on this three-body reaction from a non-time-resolved experiment. By utilizing the high electron energy resolution in a synchrotron-based Auger-electron multi-ion coincidence measurement, the dependence of the time-scale of this unimolecular reaction on the available internal energy was revealed. We observed that the reaction model approached that of secondary dissociation at low available energies near the appearance energy of this dissociation pathway. In the analysis using the generalized secondary dissociation model, and connecting it to the momentum correlations in the PIPICO patterns of (R^+,I^+), we determined the longest secondary ionization time between the separation of charged and neutral iodines to be 1.5 ps when the internal energy was less than 6 eV. As the energy increased, the secondary dissociation time decreased rapidly, reaching the shortest experimental value of 129 fs at the internal energy of 11 eV just before this dissociation pathway was quenched by other, more energetic pathways. Thus, over the energy range of this pathway, more than tenfold

increase of the reaction speed occurred, moving closer to the concerted dissociation dynamics.

The experimental results were compared to the statistical analysis of stochastic charge-hopping molecular mechanics simulations. Somewhat unexpectedly, given the simplicity of the description of the molecular environment, the model gave results with a fair quantitative agreement with the experiment. This suggests that the timescales of such unimolecular reactions, although very sensitive to the initial conditions, do not require accurate details of the electronic structure for modeling. Instead, in a molecule of this size, inclusion of the available energy in the form of internal temperature leads to a reasonable representation of the timescales of the bond-breaks. In other words, the molecule's ability to contain the energy in the reservoir of its vibrational degrees of freedom over a statistical, energy-dependent time period appears to be a key factor.

Such reconstructions of early dissociation events and timescales from energy-resolved multi-particle coincidence experiments, based on the accumulated momentum "history" of fragments, can be a valuable complement to time-resolved experiments as they can be combined with a precise control over the initial conditions at the onset of the molecular dynamics that is achievable in experiments at synchrotron radiation sources.

Conflicts of interest

There are no conflicts to declare.

Acknowledgements

EK acknowledges funding by the Academy of Finland. LP acknowledges financial support from The Vilho, Yrjö and Kalle Väisälä Foundation of the Finnish Academy of Science and Letters. SM acknowledges financial support from Knut and Alice Wallenberg Foundation and the COST Action CA18212 – Molecular Dynamics in the GAS phase (MD-GAS), supported by COST (European Cooperation in Science and Technology). KK acknowledges funding by Academy of Finland and Estonian Research Council (grant PRG551). We acknowledge MAX IV Laboratory for time on Beamline FinEstBeAMS under proposal 20190446. Research conducted at MAX IV, a Swedish national user facility, is supported by the Swedish Research council under contract 2018-07152, the Swedish Governmental Agency for Innovation Systems under contract 2018-04969, and Formas under contract 2019-02496. We also thank Dr J. Niskanen for fruitful scientific discussions on the topic.

References

1 L. Young, K. Ueda, M. Gühr, P. H. Bucksbaum, M. Simon, S. Mukamel, N. Rohringer, K. C. Prince, C. Masciovecchio, M. Meyer, A. Rudenko, D. Rolles, C. Bostedt, M. Fuchs, D. A. Reis, R. Santra, H. Kapteyn, M. Murnane, H. Ibrahim, F. Légaré, M. Vrakking, M. Isinger, D. Kroon, M. Gisselbrecht, A. LHuillier, H. J. Wörner and S. R. Leone, *J. Phys. B: At., Mol. Opt. Phys.*, 2018, **51**, 032003.
2 N. Berrah, *Phys. Scr.*, 2016, **T169**, 014001.
3 C. Milne, T. Penfold and M. Chergui, *Coord. Chem. Rev.*, 2014, **277–278**, 44–68.
4 J. W. McManus, T. Walmsley, K. Nagaya, J. R. Harries, Y. Kumagai, H. Iwayama, M. N. Ashfold, M. Britton, P. H. Bucksbaum, B. Downes-Ward, T. Driver, D. Heathcote, P. Hockett, A. J. Howard, E. Kukk, J. W. L. Lee, Y. Liu, D. Milesevic, R. S. Minns, A. Niozu, J. Niskanen, A. J. Orr-Ewing, S. Owada, D. Rolles, P. A. Robertson, A. Rudenko, K. Ueda, J. Unwin, C. Vallance, M. Burt, M. Brouard, R. Forbes and F. Allum, *Phys. Chem. Chem. Phys.*, 2022, **24**, 22699–22709.
5 E. Kukk, H. Fukuzawa, J. Niskanen, K. Nagaya, K. Kooser, D. You, J. Peschel, S. Maclot, A. Niozu and S. Saito, *Phys. Rev. Res.*, 2021, **3**, 013221.
6 T. Jahnke, R. Guillemin, L. Inhester, S.-K. Son, G. Kastirke, M. Ilchen, J. Rist, D. Trabert, N. Melzer, N. Anders, T. Mazza, R. Boll, A. De Fanis, V. Music, T. Weber, M. Weller, S. Eckart, K. Fehre, S. Grundmann, A. Hartung, M. Hofmann, C. Janke, M. Kircher, G. Nalin, A. Pier, J. Siebert, N. Strenger, I. Vela-Perez, T. Baumann, P. Grychtol, J. Montano, Y. Ovcharenko, N. Rennhack, D. Rivas, R. Wagner, P. Ziolkowski, P. Schmidt, T. Marchenko, O. Travnikova, L. Journel, I. Ismail, E. Kukk, J. Niskanen, F. Trinter, C. Vozzi, M. Devetta, S. Stagira, M. Gisselbrecht, A. Jäger, X. Li, Y. Malakar, M. Martins, R. Feifel, L. Schmidt, A. Czasch, G. Sansone, D. Rolles, A. Rudenko, R. Moshammer, R. Dörner, M. Meyer, T. Pfeifer, M. Schöffler, R. Santra, M. Simon and M. Piancastelli, *Phys. Rev. X*, 2021, **11**, 041044.
7 K. Ueda, E. Sokell, S. Schippers, F. Aumayr, H. Sadeghpour, J. Burgdörfer, C. Lemell, X.-M. Tong, T. Pfeifer, F. Calegari, A. Palacios, F. Martin, P. Corkum, G. Sansone, E. V. Gryzlova, A. N. Grum-Grzhimailo, M. N. Piancastelli, P. M. Weber, T. Steinle, K. Amini, J. Biegert, N. Berrah, E. Kukk, R. Santra, A. Müller, D. Dowek, R. R. Lucchese, C. W. McCurdy, P. Bolognesi, L. Avaldi, T. Jahnke, M. S. Schöffler, R. Dörner, Y. Mairesse, L. Nahon, O. Smirnova, T. Schlathölter, E. E. B. Campbell, J.-M. Rost, M. Meyer and K. A. Tanaka, *J. Phys. B: At., Mol. Opt. Phys.*, 2019, **52**, 171001.
8 P. Çarçabal, D. Descamps, S. Petit, Y. Mairesse, V. Blanchet and R. Cireasa, *Faraday Discuss.*, 2016, **194**, 407–425.
9 R. Geneaux, H. J. B. Marroux, A. Guggenmos, D. M. Neumark and S. R. Leone, *Philos. Trans. R. Soc., A*, 2019, **377**, 20170463.
10 N. Hartmann, S. Bhattacharyya, F. Schlaepfer, M. Volkov, Z. Schumacher, M. Lucchini, L. Gallmann, U. Rothlisberger and U. Keller, *Phys. Chem. Chem. Phys.*, 2019, **21**, 18380–18385.
11 A. Boyer, M. Hervé, V. Despré, P. Castellanos Nash, V. Loriot, A. Marciniak, A. Tielens, A. Kuleff and F. Lépine, *Phys. Rev. X*, 2021, **11**, 041012.
12 A. Boyer, M. Hervé, A. Scognamiglio, V. Loriot and F. Lépine, *Phys. Chem. Chem. Phys.*, 2021, **23**, 27477–27483.
13 F. Lépine, M. Y. Ivanov and M. J. J. Vrakking, *Nat. Photonics*, 2014, **8**, 195–204.
14 S. Maclot, J. Lahl, J. Peschel, H. Wikmark, P. Rudawski, F. Brunner, H. Coudert-Alteirac, S. Indrajith, B. A. Huber,

S. Díaz-Tendero, N. F. Aguirre, P. Rousseau and P. Johnsson, *Sci. Rep.*, 2020, **10**, 2884.

15 H. Köckert, J. W. L. Lee, F. Allum, K. Amini, S. Bari, C. Bomme, F. BrauÃŸe, M. Brouard, M. Burt, B. Cunha de Miranda, S. Düsterer, P. Eng-Johnsson, B. Erk, M. Géléoc, R. Geneaux, A. S. Gentleman, R. Guillemin, G. Goldsztejn, D. M. P. Holland, I. Ismail, L. Journel, T. Kierspel, J. Küpper, J. Lahl, S. R. Mackenzie, S. Maclot, B. Manschwetus, A. S. Mereshchenko, T. Mullins, P. K. Olshin, J. Palaudoux, F. Penent, M. N. Piancastelli, D. Rompotis, A. Rouzée, T. Ruchon, A. Rudenko, N. Schirmel, M. Simon, S. Techert, O. Travnikova, S. Trippel, C. Vallance, E. Wang, J. Wiese, F. Ziaee, T. Marchenko, D. Rolles and R. Boll, *J. Phys. B: At., Mol. Opt. Phys.*, 2022, **55**, 014001.

16 T. Arion and U. Hergenhahn, *J. Electron Spectrosc. Relat. Phenom.*, 2015, **200**, 222–231.

17 M. Wöstmann, R. Mitzner, T. Noll, S. Roling, B. Siemer, F. Siewert, S. Eppenhoff, F. Wahlert and H. Zacharias, *J. Phys. B: At., Mol. Opt. Phys.*, 2013, **46**, 164005.

18 N. Berrah, L. Fang, B. F. Murphy, E. Kukk, T. Y. Osipov, R. Coffee, K. R. Ferguson, H. Xiong, J.-C. Castagna, V. S. Petrovic, S. C. Montero and J. D. Bozek, *Opt. Express*, 2016, **24**, 11768.

19 S. Serkez, W. Decking, L. Froehlich, N. Gerasimova, J. Grünert, M. Guetg, M. Huttula, S. Karabekyan, A. Koch, V. Kocharyan, Y. Kot, E. Kukk, J. Laksman, P. Lytaev, T. Maltezopoulos, T. Mazza, M. Meyer, E. Saldin, E. Schneidmiller, M. Scholz, S. Tomin, M. Vannoni, T. Wohlenberg, M. Yurkov, I. Zagorodnov and G. Geloni, *Appl. Sci.*, 2020, **10**, 2728.

20 G. Lanzani, G. Cerullo, S. Stagira and S. De Silvestri, *J. Photochem. Photobiol., A*, 2001, **144**, 13–19.

21 R. Weinkauf, L. Lehr, E. W. Schlag, S. Salzmann and C. M. Marian, *Phys. Chem. Chem. Phys.*, 2008, **10**, 393–404.

22 S. Salzmann, M. Kleinschmidt, J. Tatchen, R. Weinkauf and C. M. Marian, *Phys. Chem. Chem. Phys.*, 2008, **10**, 380–392.

23 P. Kölle, T. Schnappinger and R. de Vivie-Riedle, *Phys. Chem. Chem. Phys.*, 2016, **18**, 7903–7915.

24 E. Kukk, D. T. Ha, Y. Wang, D. G. Piekarski, S. Diaz-Tendero, K. Kooser, E. Itälä, H. Levola, M. Alcamí, E. Rachlew and F. Martín, *Phys. Rev. A: At., Mol., Opt. Phys.*, 2015, **91**, 043417.

25 T. Schnappinger, P. Kölle, M. Marazzi, A. Monari, L. González and R. de Vivie-Riedle, *Phys. Chem. Chem. Phys.*, 2017, **19**, 25662–25670.

26 S. Pathak, L. M. Ibele, R. Boll, C. Callegari, A. Demidovich, B. Erk, R. Feifel, R. Forbes, M. Di Fraia, L. Giannessi, C. S. Hansen, D. M. P. Holland, R. A. Ingle, R. Mason, O. Plekan, K. C. Prince, A. Rouzée, R. J. Squibb, J. Tross, M. N. R. Ashfold, B. F. E. Curchod and D. Rolles, *Nat. Chem.*, 2020, **12**, 795–800.

27 L. Pihlava, J. Niskanen, K. Kooser, C. StrÅhlman, S. Maclot, A. Kivimäki and E. Kukk, *Phys. Chem. Chem. Phys.*, 2021, **23**, 21249.

28 G. Turkoglu, M. E. Cinar and T. Ozturk, *Top. Curr. Chem.*, 2017, **375**, 84.

29 L. Vallan, E. Istif, I. J. Gómez, N. Alegret and D. Mantione, *Polymers*, 2021, **13**, 1977.

30 T. Yamamoto, *NPG Asia Mater.*, 2010, **2**, 54–60.

31 B. Capozzi, E. J. Dell, T. C. Berkelbach, D. R. Reichman, L. Venkataraman and L. M. Campos, *J. Am. Chem. Soc.*, 2014, **136**, 10486–10492.

32 D. You, H. Fukuzawa, Y. Luo, S. Saito, M. Berholts, T. Gaumnitz, M. Huttula, P. Johnsson, N. Kishimoto, H. Myllynen, A. Nemer, A. Niozu, M. Patanen, E. Pelimanni, T. Takanashi, S.-I. Wada, N. Yokono, S. Owada, K. Tono, M. Yabashi, K. Nagaya, E. Kukk and K. Ueda, *Phys. Chem. Chem. Phys.*, 2019, **22**, 2648–2659.

33 S. Makurat, P. Spisz, W. Kozak, J. Rak and M. Zdrowowicz, *Int. J. Mol. Sci.*, 2019, **20**, 1308.

34 T. Takanashi, K. Nakamura, E. Kukk, K. Motomura, H. Fukuzawa, K. Nagaya, S.-I. Wada, Y. Kumagai, D. Iablonskyi, Y. Ito, Y. Sakakibara, D. You, T. Nishiyama, K. Asa, Y. Sato, T. Umemoto, K. Kariyazono, K. Ochiai, M. Kanno, K. Yamazaki, K. Kooser, C. Nicolas, C. Miron, T. Asavei, L. Neagu, M. Schöffler, G. Kastirke, X.-J. Liu, A. Rudenko, S. Owada, T. Katayama, T. Togashi, K. Tono, M. Yabashi, H. Kono and K. Ueda, *Phys. Chem. Chem. Phys.*, 2017, **19**, 19707–19721.

35 R. Boll, B. Erk, R. Coffee, S. Trippel, T. Kierspel, C. Bomme, J. D. Bozek, M. Burkett, S. Carron, K. R. Ferguson, L. Foucar, J. Küpper, T. Marchenko, C. Miron, M. Patanen, T. Osipov, S. Schorb, M. Simon, M. Swiggers, S. Techert, K. Ueda, C. Bostedt, D. Rolles and A. Rudenko, *Struct. Dyn.*, 2016, **3**, 043207.

36 K. Motomura, E. Kukk, H. Fukuzawa, S.-I. Wada, K. Nagaya, S. Ohmura, S. Mondal, T. Tachibana, Y. Ito, R. Koga, T. Sakai, K. Matsunami, A. Rudenko, C. Nicolas, X.-J. Liu, C. Miron, Y. Zhang, Y. Jiang, J. Chen, M. Anand, D. E. Kim, K. Tono, M. Yabashi, M. Yao and K. Ueda, *J. Phys. Chem. Lett.*, 2015, **6**, 2944–2949.

37 B. Erk, R. Boll, S. Trippel, D. Anielski, L. Foucar, B. Rudek, S. W. Epp, R. Coffee, S. Carron, S. Schorb, K. R. Ferguson, M. Swiggers, J. D. Bozek, M. Simon, T. Marchenko, J. Kupper, I. Schlichting, J. Ullrich, C. Bostedt, D. Rolles and A. Rudenko, *Science*, 2014, **345**, 288–291.

38 K. Nagaya, K. Motomura, E. Kukk, H. Fukuzawa, S. Wada, T. Tachibana, Y. Ito, S. Mondal, T. Sakai, K. Matsunami, R. Koga, S. Ohmura, Y. Takahashi, M. Kanno, A. Rudenko, C. Nicolas, X.-J. Liu, Y. Zhang, J. Chen, M. Anand, Y. Jiang, D.-E. Kim, K. Tono, M. Yabashi, H. Kono, C. Miron, M. Yao and K. Ueda, *Phys. Rev. X*, 2016, **6**, 21035.

39 L. Fang, H. Xiong, E. Kukk and N. Berrah, *Appl. Sci.*, 2017, **7**, 529.

40 F. Allum, M. Burt, K. Amini, R. Boll, H. Köckert, P. K. Olshin, S. Bari, C. Bomme, F. BrauÃŸe, B. Cunha de Miranda, S. Düsterer, B. Erk, M. Géléoc, R. Geneaux, A. S. Gentleman, G. Goldsztejn, R. Guillemin, D. M. P. Holland, I. Ismail, P. Johnsson, L. Journel, J. Küpper, J. Lahl, J. W. L. Lee, S. Maclot, S. R. Mackenzie, B. Manschwetus, A. S. Mereshchenko, R. Mason, J. Palaudoux, M. N. Piancastelli, F. Penent, D. Rompotis, A. Rouzée, T. Ruchon, A. Rudenko, E. Savelyev, M. Simon, N. Schirmel, H. Stapelfeldt, S. Techert, O. Travnikova, S. Trippel, J. G. Underwood, C. Vallance, J. Wiese, F. Ziaee, M. Brouard, T. Marchenko and D. Rolles, *J. Chem. Phys.*, 2018, **149**, 204313.

41 R. Pärna, R. Sankari, E. Kukk, E. Nõmmiste, M. Valden, M. Lastusaari, K. Kooser, K. Kokko, M. Hirsimäki, S. Urpelainen, P. Turunen, A. Kivimäki, V. Pankratov, L. Reisberg, F. Hennies, H. Tarawneh, R. Nyholm and M. Huttula, *Nucl. Instrum. Methods Phys. Res., Sect. A*, 2017, **859**, 83–89.

42 K. Chernenko, A. Kivimäki, R. Pärna, W. Wang, R. Sankari, M. Leandersson, H. Tarawneh, V. Pankratov, M. Kook, E. Kukk, L. Reisberg, S. Urpelainen, T. Käämbre, F. Siewert, G. Gwalt, A. Sokolov, S. Lemke, S. Alimov, J. Knedel, O. Kutz, T. Seliger, M. Valden, M. Hirsimäki, M. Kirm and M. Huttula, *J. Synchrotron Radiat.*, 2021, **28**, 1620–1630.

43 K. Kooser, A. Kivimäki, P. Turunen, R. Pärna, L. Reisberg, M. Kirm, M. Valden, M. Huttula and E. Kukk, *J. Synchrotron Radiat.*, 2020, **27**, 1080–1091.

44 G. Prümper and K. Ueda, *Nucl. Instrum. Methods Phys. Res., Sect. A*, 2007, **574**, 350–362.

45 E. Kukk, H. Myllynen, K. Nagaya, S. Wada, J. D. Bozek, T. Takanashi, D. You, A. Niozu, K. Kooser, T. Gaumnitz, E. Pelimanni, M. Berholts, S. Granroth, N. Yokono, H. Fukuzawa, C. Miron and K. Ueda, *Phys. Rev. A*, 2019, **99**, 023411.

46 D. Marx and J. Hutter, *Ab Initio Molecular Dynamics: Basic Theory and Advanced Methods*, Cambridge University Press, 1st edn, 2009.

47 N. Sakhaee, S. Sakhaee, E. Doustkhah and A. Mobaraki, *Curr. Organocatal.*, 2021, **8**, 228–237.

48 Z. Li, L. Inhester, C. Liekhus-Schmaltz, B. F. E. Curchod, J. W. Snyder, N. Medvedev, J. Cryan, T. Osipov, S. Pabst, O. Vendrell, P. Bucksbaum and T. J. Martinez, *Nat. Commun.*, 2017, **8**, 453.

49 D. T. Ha, K. Yamazaki, Y. Wang, M. Alcamí, S. Maeda, H. Kono, F. Martin and E. Kukk, *J. Chem. Phys.*, 2016, **145**, 094302.

50 B. Marchetti, T. N. V. Karsili, O. Kelly, P. Kapetanopoulos and M. N. R. Ashfold, *J. Chem. Phys.*, 2015, **142**, 224303.

51 V. S. Petrović, M. Siano, J. L. White, N. Berrah, C. Bostedt, J. D. Bozek, D. Broege, M. Chalfin, R. N. Coffee, J. Cryan, L. Fang, J. P. Farrell, L. J. Frasinski, J. M. Glownia, M. Gühr, M. Hoener, D. M. P. Holland, J. Kim, J. P. Marangos, T. Martinez, B. K. McFarland, R. S. Minns, S. Miyabe, S. Schorb, R. J. Sension, L. S. Spector, R. Squibb, H. Tao, J. G. Underwood and P. H. Bucksbaum, *Phys. Rev. Lett.*, 2012, **108**, 253006.